

# Active control of internal transport barrier formation due to off-axis electron-cyclotron heating in GAMMA 10 experiments<sup>a)</sup>

T. Cho,<sup>b)</sup> V. P. Pastukhov,<sup>c)</sup> W. Horton,<sup>d)</sup> T. Numakura, M. Hirata, J. Kohagura, N. V. Chudin,<sup>c)</sup> and J. Pratt<sup>d)</sup>

Plasma Research Centre, University of Tsukuba, Tsukuba, Ibaraki 305-8577, Japan

(Received 13 November 2007; accepted 17 March 2008; published online 7 May 2008)

The controlled formation of an internal transport barrier (ITB) is observed in GAMMA 10 [T. Cho *et al.*, Nucl. Fusion **45**, 1650 (2005)]. The barrier is localized within a layer of a strongly sheared  $E_r \times B$  plasma rotation ( $5.5 < r_c \leq 10$  cm). This high-vorticity layer is formed and maintained by off-axis electron-cyclotron heating, which generates a cylindrical layer ( $4 < r_c < 7$  cm) with a high-energy electron population that modifies the initial Gaussian radial potential profile into a nonmonotonic one with a hump structure. The local gradients of  $T_i$  and  $T_e$  are appreciably enhanced in the ITB layer, similarly to those of the ITB in tokamaks and stellarators. Reductions in the effective ion and electron thermal diffusivities are obtained in the barrier layer. A reduction of the observed low-frequency turbulence in the ITB layer and a partial decoupling of the turbulent structures localized on either side of the layer are demonstrated by two-dimensional x-ray diagnostics. © 2008 American Institute of Physics. [DOI: 10.1063/1.2906262]

## I. INTRODUCTION

Anomalous particle and energy cross-field transport is one of the most critical issues in magnetic plasma confinement for fusion, as well as in the physics of magnetized plasmas in general. In magnetic confinement systems with different magnetic-field topologies (e.g., tokamaks,<sup>1</sup> stellarators,<sup>2</sup> and mirrors<sup>3-6</sup>), recent experiments have shown that low-frequency (LF) turbulence and the associated anomalous cross-field plasma transport exhibit rather common features including high-confinement mode transitions and internal transport-barrier (ITB) formation.

According to conventional theories,<sup>7,8</sup>  $E \times B$  sheared flows can strongly distort turbulent vortexlike structures and reduce the radial coherence length of the turbulence, and transport-barrier formation in the sheared-flow layer is expected. Flow-shear-induced transport barriers have been experimentally observed in toroidal plasmas in various situations.<sup>1,2,9-11</sup> Suppression of intermittent turbulent vortexlike structures due to strongly sheared plasma rotation were observed in GAMMA 10.<sup>3,4</sup> In those experiments, turbulence suppression was observed after the application of electron-cyclotron heating (ECH) in the plug and barrier regions in association with the central-cell potential rise and an increase in the radial electric fields  $E_r$  for  $E_r \times B$  sheared flow enhancement.

Recently, observations of controlled ITB formation in GAMMA 10 have been briefly presented in papers.<sup>5,6</sup> The main features<sup>3-6</sup> of LF turbulence and the associated anomalous cross-field transport in GAMMA 10 are similar to those in other magnetic confinement systems in spite of the differ-

ent topologies. Moreover, the difference in topology between GAMMA 10 and axisymmetric toroidal systems is not as crucial for the problem of cross-field transport as it looks from a *prima impressionis*. On the other hand, mirror devices having open magnetic-field lines provide intrinsic advantages for the control of radial potential profiles by means of end-plate biasing and/or the modification of axial particle-loss balance, due to electron-loss control by ECH for instance.<sup>3-6,12</sup> Therefore, mirror-based systems can be considered to be quite flexible for the experimental study of the influence of sheared flows on LF turbulence and the associated anomalous cross-field transport in magnetized plasmas. The controlled modification of sheared-flow profiles by the off-axis ECH described in this paper is a new promising method of studying flow-shear-induced transport-barrier formation. The present paper gives an extended presentation of the results for actively controlled ITB in GAMMA 10.

## II. EXPERIMENTAL APPARATUS AND DIAGNOSTIC METHODS

GAMMA 10,<sup>3-6</sup> which is a minimum- $B$  anchored tandem mirror with an outboard axisymmetric plug and barrier cells, has an axial length ( $L_z$ ) of 27 m, and a vacuum vessel of 150 m<sup>3</sup> [Fig. 1]. In the central cell [ $L_z=6$  m; limiter diameter=36 cm; magnetic fields  $B_z=B_m$  at the 0.405-T mid-plane; mirror ratio ( $R_m$ )=5.2], ion cyclotron heating (30 kW at 6.36 MHz for central-cell hot-ion production; 30 kW at 9.9 or 10.3 MHz for anchor-cell stabilization) is applied. The plug and barrier cells are axisymmetric mirrors with  $L_z=2.5$  m,  $B_m=0.497$  T, and  $R_m=6.2$  for standard operations. In the transport-barrier experiments, a 4.75% higher  $B_m$  (0.519 T) is applied in the barrier cell for off-axis resonant ECH to produce the cylindrical energetic-electron layer. A gyrotron power of 120 kW at 28 GHz is injected into a single (east) barrier cell alone to produce the layer. No additional ECH is applied, thereby simplifying the experimental

<sup>a)</sup>Paper G12 6, Bull. Am. Phys. Soc. **52**, 100 (2007).

<sup>b)</sup>Invited speaker.

<sup>c)</sup>Permanent address: Russian Research Center, "Kurchatov Institute," Moscow, Russia.

<sup>d)</sup>Permanent address: Institute for Fusion Studies, University of Texas at Austin, USA.

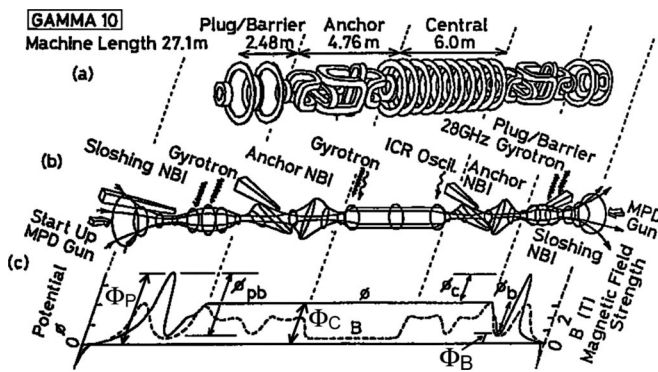


FIG. 1. Schematic view of GAMMA 10: (a) Magnetic coil set, (b) magnetic flux tube with heating systems, and (c) axial magnetic field (dashed curve) and potential profiles (solid curve).

situations for electron transport analysis (see Sec. IV). In standard operations with central-cell ECH (250 kW) [ $T_e \approx 750$  eV], as well as both plug and barrier ECH for an ion-confining potential  $\phi_c$  formation of 3 kV,<sup>6</sup> strong sheared flows are maintained at all radii. In this paper, however, we focus on the transport-barrier control and the effects under simplified operational conditions with only the single-barrier ECH.

Various fluctuation diagnostics, which include a movable microwave interferometer, two sets of 50-channel soft x-ray tomography detectors with microchannel plates<sup>3-6,13</sup> in the central-cell midplane, several semiconductor detectors in various cells for  $T_e$  and  $T_i$  diagnostics,<sup>3-6,14-16</sup> heavy-ion ( $\text{Au}^0$ ) beam probes (HIBPs)<sup>17</sup> and four sets of electrostatic ion-energy-spectrometer (IES ELA) arrays,<sup>18</sup> are employed. Energetic electron currents are observed by using a radially movable conventional end-loss analyzer (a movable IES ELA)<sup>18,19</sup> at the west end. The central-cell potentials  $\Phi_C$  and the barrier potentials  $\Phi_B$  are directly measured by means of HIBP. The  $\Phi_C$  values are also obtained using IES ELA arrays and movable IES ELA due to end-loss-ion energy analyses.<sup>3-6,18-20</sup> Simultaneous potential diagnostics with HIBP and IES ELA show consistent characteristics.

### III. SHEARED $E \times B$ ROTATION AND TURBULENCE IN REGIMES WITH OFF-AXIS RESONANT ECH

Studies of the physical mechanism of the influence of sheared flows on a well-developed intermittent LF turbulence are carried out in the hot-ion mode of GAMMA 10<sup>3-6</sup> under the following simplified conditions. A moderate off-axis resonant ECH (120 kW) without other ECH is applied at the barrier region to modify the radial plasma potential profile. The off-axis barrier ECH ( $t > 149.2$  ms) produces a small population ( $\approx 10^{-5}$  of the total central-cell density  $n_c$ ) of high-energy electrons ( $\approx 2$  keV) localized in a cylindrical layer ( $4 < r_c < 7$  cm) formed along the whole device [see Fig. 2(a)]. No beta-value effects or negligible plasma heating are anticipated under such parameters of the hot-electron population. However, the population of hot electrons changes the balance of particle loss within the layer along the magnetic flux tube connected with coaxial end plates. Hence, the

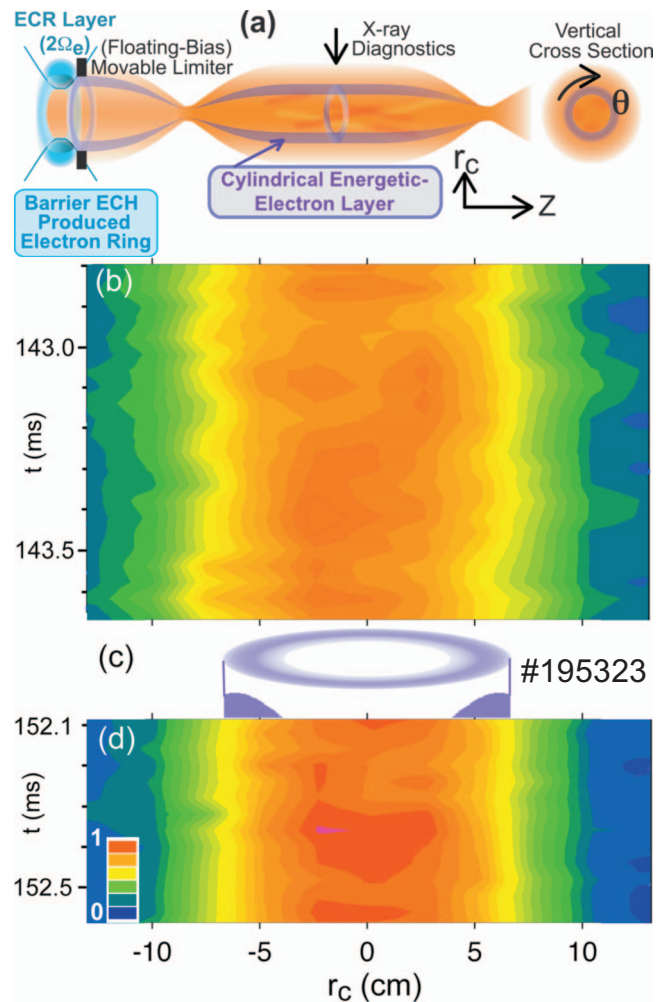


FIG. 2. (Color) (a) Experimental configuration of radial transport-barrier formation using off-axis barrier ECH. The contours of the central-cell x-ray brightness are shown in (b) the presence and (d) absence of (c) a cylindrical shaped energetic-electron layer produced by the off-axis ECH. The hot-colored areas show locations with higher plasma pressure. Strong turbulence with vortexlike structures exist at  $r_c < 4$  cm in (b) and (d). However, its quietly suppressed region in (d) is observed both in the layer and the externally surrounding cylindrical layer ( $5.5 < r_c \leq 10$  cm). ( $I \propto n_e n_i T_e^{2.3}$ .)

loss of a small fraction of hot electrons modifies the initial radial potential profile, changing it into a radially nonmonotonic one with a hump at  $r_c \approx 7$  cm. This positively humped potential profile induces a strongly sheared  $E \times B$  plasma rotation in the cylindrical layer ( $5.5 < r_c \leq 10$  cm) near the potential hump-top along the whole device, since the positive and the negative gradient  $\Phi_C$  on each side of the  $\Phi_C$  hump at  $r_c$  provides the oppositely directed  $E \times B$  rotational flow.

To investigate the effects of the energetic-electron layer on the behavior and structure of turbulent plasmas (Fig. 2), the contours of the central-cell soft x-ray brightness, i.e.,  $I_{\text{SX}}$ , are shown before and during the barrier ECH [see, respectively, Figs. 2(b) and 2(d)]. In the internal region ( $r_c < 5$  cm) having higher plasma pressure, spatially and temporally varying intermittently turbulent vortexlike structures are evident [Figs. 2(b) and 2(d)]. Without the layer, turbulent fluctuations, driven from the internal region, extend through the entire radial scale, as seen in Fig. 2(b), particularly at  $t \approx 142.85, 143.1,$  and  $143.4$  ms. The formation of the

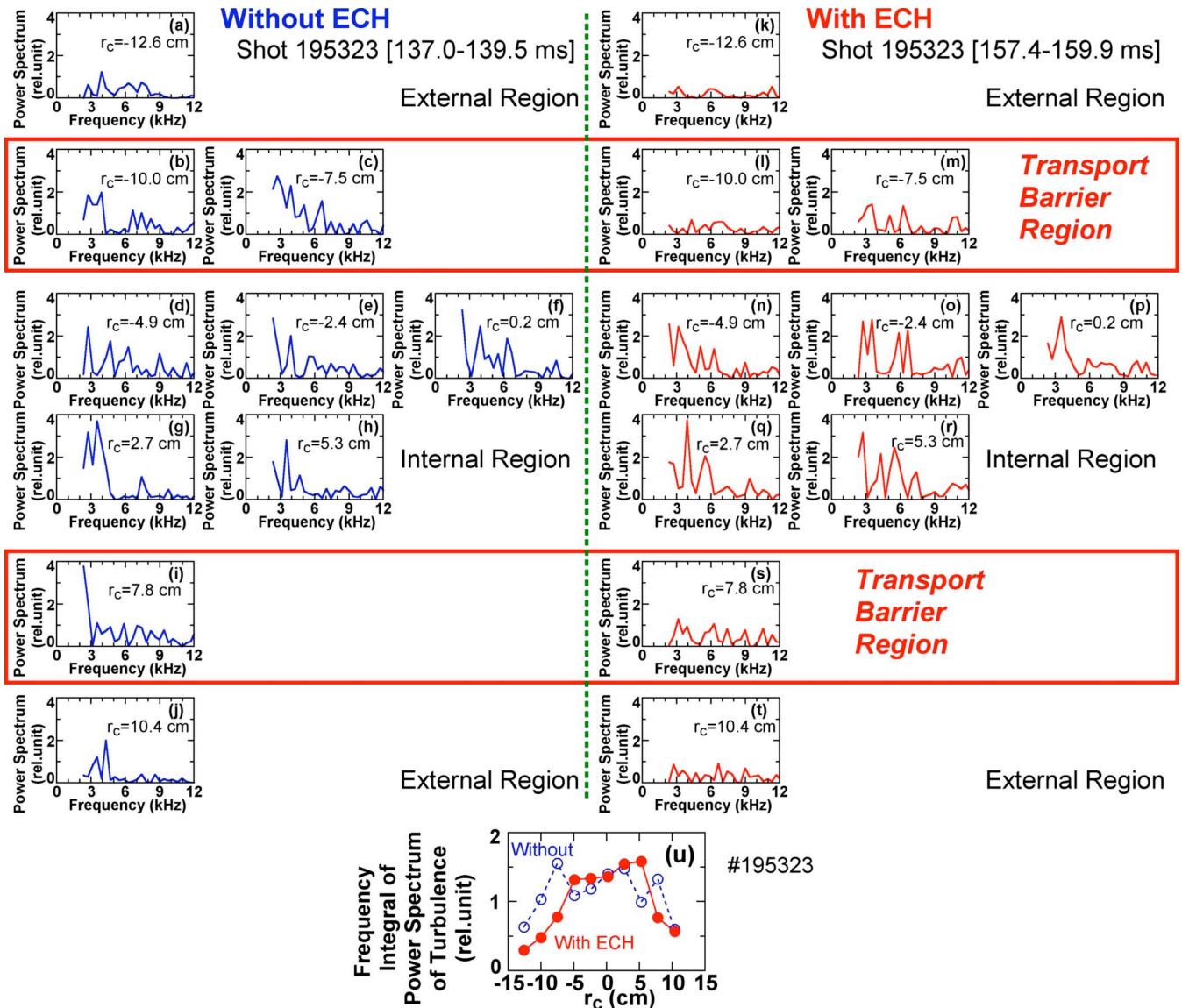


FIG. 3. (Color online) The Fourier power spectra of the x-ray data are obtained during  $t=137.0\text{--}139.5$  ms [(a)–(j)], and  $157.4\text{--}159.9$  ms [(k)–(t)] at the same shot No. 195323 as in Fig. 2. The frequency-integrated total amplitude over 2–10 kHz is shown in (u), where the open and filled circles show the cases without and with the layer, respectively. The spectra are calculated using the rectangular window function. In addition to Fig. 2(d), the spectra in (l), (m), and (s) ( $5.5 < r_c \leq 10$  cm) show in particular the reduction of the low-frequency (LF) part ( $< 5$  kHz) of the turbulence, as compared to those in (b), (c), and (i). In the internal region, almost no changes in the spectral characteristics, including the LF regime are seen, in either (d)–(h) or (n)–(r).

sheared-rotation layer results in a considerable reduction of turbulence within the layer ( $5.5 < r_c \leq 10$  cm) and its mitigation in the external region ( $r_c > 10$  cm), so that strong fluctuations in the core do not continuously extend through the layer [Fig. 2(d)]. In this region, small temporal variations of the contours (i.e., contours directed almost in parallel to the  $t$  axis having quite small radially fluctuating turbulent structures with time) are seen [Fig. 2(d)]. Here, a plasma discharge shot number 195323 is employed.

For reference, this property has also been found in the following alternative analyses. The widely employed Fourier power spectra<sup>21–23</sup> (i.e., the square of the linear spectral intensities<sup>5</sup>) of the x rays are compared without and with the ECH-produced energetic-electron layer. After  $t=149.2$  ms, ECH is injected. Figures 3(a)–3(t) show the data obtained during  $t=137.0\text{--}139.5$  ms and  $157.4\text{--}159.9$  ms at shot No.

195323, respectively, along with the radial plots of the frequency-integrated total amplitude of each power spectrum<sup>21</sup> over 2–10 kHz [see Fig. 3(u), where the open and filled circles show the case without and with the layer, respectively]. The Fourier power spectra are calculated using the “rectangular window” function.<sup>21</sup> The alternative use of the “Welch window” function and so on<sup>21</sup> consistently shows the similar amplitude reduction both within the layer and in the external region. (See the reduction in  $< 5$  kHz.)

In addition to the visible two-dimensional x-ray data in Fig. 2(d) at the same shot, a reduction of turbulence in the layer can also be seen when comparing Figs. 3(b), 3(c), and 3(i) and Figs. 3(l), 3(m), and 3(s) for  $5.5 < r_c \leq 10$  cm (compare the data in Figs. 2(d) and 3 also). For the x-ray contour data in the quietly stabilized region in Fig. 2(d), the power spectra in Figs. 3(l), 3(m), and 3(s) give detailed information

on the mitigation of the low-frequency part of the turbulence.

In the internal region surrounded by the layer [compare Figs. 3(d)–3(h) with Figs. 3(n)–3(r)], almost no changes in the frequency-spectrum characteristics including the low-frequency properties are seen in either the case with layer formation or that without. The frequency-integrated power spectrum of the turbulence in this internal region tends to behave randomly or increase somewhat with the energetic-layer formation. This tendency apparent in these two regions is reproduced at the other plasma shots and over various time durations. In Fig. 3(u), the asymmetry of the integrated amplitude at  $r_c$  may have been due to the short sampling duration as compared to the averaged characteristic rotational time of intermittent turbulence, which is smoothed out symmetrically. Further, it should be noted that the superimposition of short-time but intense bursts extending beyond the layer [see, for instance, the data at 152.3 ms in Fig. 2(d)] significantly disturbs and enhances the actually quiet signals at the edge region [compare the data in Figs. 3(a) and 3(k), Figs. 3(j) and 3(t), or Figs. 4(d) and 4(h) with those having the clearer difference in Figs. 2(b) and 2(d) at the edge region]. The essential role of the transport-barrier formation is thus to reduce turbulence in the strong sheared layer.

The Fourier power spectra from the IES ELA array at  $r_c=2.6$  [Figs. 4(a) and 4(e)], 5.3 [Figs. 4(b) and 4(f)], 8.3 [Figs. 4(c) and 4(g)], and 11.3 cm [Figs. 4(d) and 4(h)] in the absence [Figs. 4(a)–4(d)] and presence [Figs. 4(e)–4(h)] of the layer are presented. Turbulence at all radii  $r_c$  without the layer, and in the internal region surrounded by the layer are similarly observed in both cases in the x-ray and the IES ELA ion signal. On the other hand, the turbulence is significantly reduced in the layer [Fig. 4(g)]. Here, the Fourier spectra are calculated using the rectangular window function.<sup>21</sup> For a more accurate estimation, further signal contributions from the fluctuation signals due to the energetic electrons themselves in the electron layer on the IES ELA spectra shown in Figs. 4(g) and 4(h) should be subtracted from the IES ELA spectrum data, since  $\approx 3\%$  of total energetic electron flux is estimated to be incident onto the IES ELA signals in the layer. Therefore, a procedure of its subtraction from the IES ELA signals in the layer [particularly for that in Fig. 4(g)] is needed. In this case, however, it is not essential to take into account this signal reduction procedure, since a quite low-level signal is already evident in Fig. 4(g). Therefore, for simplicity, it is sufficient to demonstrate the difference between Figs. 4(c) and 4(g) without the subtraction. A plasma shot No. 195322 is used, since the shot No. 195323 is in the operational mode of potential measurement with sinusoidal ion-repeller biasing for IES ELA. The sampling durations are at  $t=144.0$ – $149.1$ , and  $150.0$ – $155.1$  ms in the case without and with the layer formation, respectively.

Consequently, in addition to the evident reduction of turbulence in the two-dimensional soft x-ray signals [Fig. 2], the frequency-integrated Fourier amplitude over the broadband turbulent fluctuations at various radii from the x-ray and IES ELA array detectors are plotted in Figs. 3(u) and 4(i), respectively. The filled and open circles in Figs. 3(u) and 4(i) correspond to the case with and without the layer,

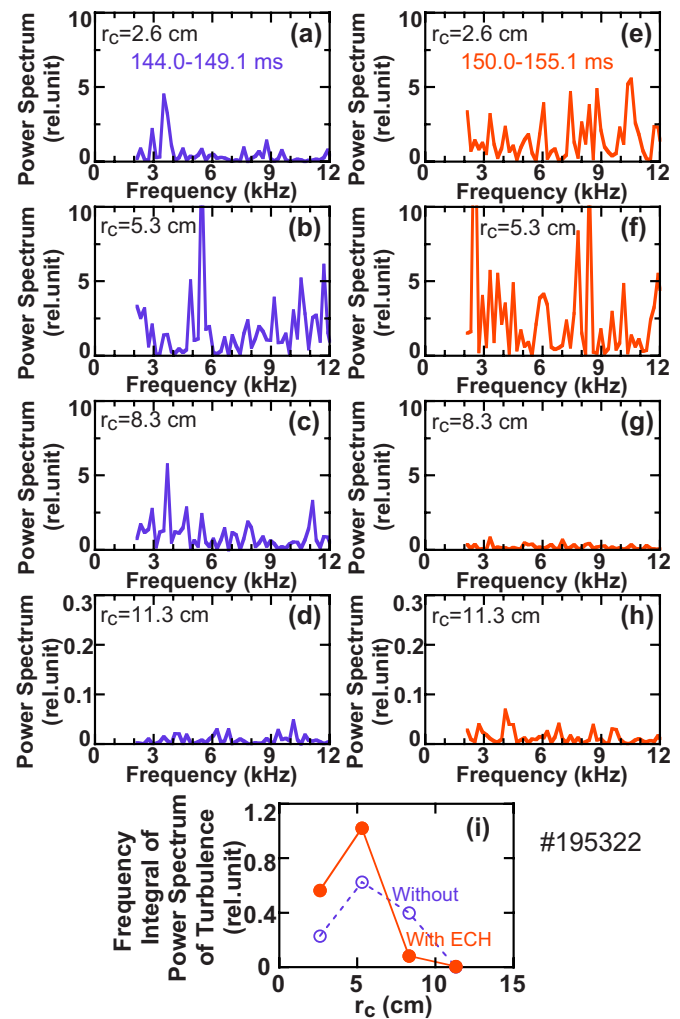


FIG. 4. (Color online) Fourier power spectra are obtained from the IES ELA array. The observation locations  $r_c$  are inserted in each figure in the case without [(a)–(d)] and with [(e)–(h)] the energetic-electron layer. The turbulence at any  $r_c$  without the layer, and that in the internal region surrounded by the layer with the layer are similarly observed for both the x-ray and the IES ELA signals. However, the turbulence is significantly reduced in the layer [see (g)]. Shot No. 195322 at  $t=144.0$ – $149.1$ , and  $150.0$ – $155.1$  ms is employed in the case without and with the layer, respectively. Here, the rectangular window function is used. For more detail, see the text.

respectively. According to these figures and Fig. 2, a mitigation of turbulent fluctuations is observed at  $5.5 < r_c \leq 10$  cm in the presence of the electron layer.

The radial profile data on  $\Phi_C$  from the central-cell HIBP (see square plots),<sup>17</sup> (west) IES ELA arrays (diamonds),<sup>18</sup> and movable IES ELA (circles)<sup>19</sup> in the presence and absence of the layer, are plotted in Fig. 5(a) using the filled and open symbols, respectively. Here, the solid and dashed curves show the  $\Phi_C$  profiles with and without the layer formation, respectively, on the basis of the regression analysis of these data. The inserted shaded regions in Figs. 2(c), 5, and 7 (see below) illustrate the location of the energetic electrons [ $4 < r_c < 7$  cm]. The electron-layer profile is found from the movable IES ELA currents, and is consistently identified upon the insertion of a radially movable metal limiter [see Fig. 2(a)] into the layer for scratching and reducing the energetic electrons in the layer, as well as through x-ray

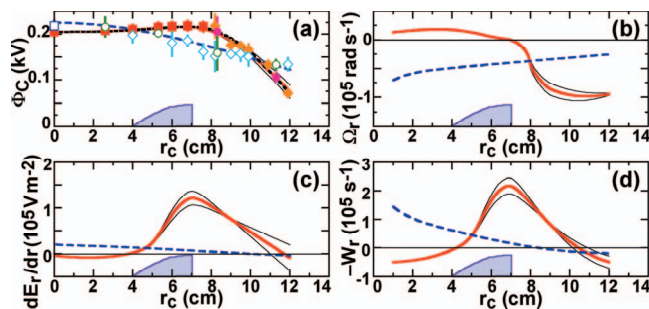


FIG. 5. (Color) (a) The radial profile data on  $\Phi_C$  from the central-cell HIBP (squares), IES ELA arrays (diamonds), and movable IES ELA (circles) along with the fitted-data solid and dashed curves resulting from the regression analysis are plotted using filled and open symbols to designate the presence and absence of the energetic-electron layer, respectively. (b) The angular velocity, which undergoes the direction reversal of the  $\mathbf{E}_r \times \mathbf{B}$  azimuthal drift flow near the hump location ( $r_c \approx 7$  cm) of (c) the  $E_r$  shear and (d) the dynamic vorticity,  $W_r$ , is plotted in the case with the layer (solid curves). The thin solid curves in (b)–(d) are calculated using the thin solid curves in (a) according to the regression analysis. Here, the set of maximum and minimum values in the estimated  $\Phi_C$  regime is used. For more detail, see the text.

profile observation with barrier x-ray tomography.<sup>24</sup> A small fraction of faster electron loss along the magnetic fields leads to the formation of a hump in the ambipolar potential, i.e.,  $\Phi_C$ , near  $r_c = 7$  cm. The black dotted curve in Fig. 5(a), which almost overlaps the red solid curve, is obtained through regression analysis using the HIBP and the IES ELA array data alone. The good agreement between the red solid and black dotted curves confirms the good reproducibility of the plasmas and the validity of each analysis method for the IES ELA array and the movable IES ELA data, since the movable ELA data are obtained with other shot-to-shot discharges. [See also the good reproducibility of the  $\Phi_C$  fitting curve with ECH in Ref. 5; i.e., the difference within 2.3% and 7.1% in the main ( $r_c < 11$  cm) and edge ( $=12$  cm) plasma regions, respectively, as compared with the fitting curve to the  $\Phi_C$  data in Fig. 5(a).]

In Fig. 6, some raw data from the IES ELA array at (b)  $r_c = 2.6$  cm, and (c) 11.3 cm without ECH as well as at (d) 11.3 cm with ECH are given as examples to enable the checking of the lowest signal level data at  $r_c = 11.3$  cm in the edge region as compared to the HIBP data with  $\approx \pm 10$  V accuracy in the higher- $n_c$  core region. According to the model function<sup>25</sup> for the observed ion signals,  $I$  (i.e., a shifted Maxwellian distribution function<sup>25</sup> described as  $I = I_0 \{1 - \exp[-e(E_i - e\Phi_C)/T_i]\}$  for  $E_i \geq e\Phi_C$ , and  $I = 0$  for  $E_i < e\Phi_C$ ), the value of  $\Phi_C$  is thereby obtained at the “rising point” of the data (see Ref. 18 for the detector characteristics). Here,  $I_0$  and  $e$  denote the incident ion current at  $E_i = \infty$  and the electronic charge, respectively.

For the digital sampling data, the “rising regime” of  $\Phi_C$  is estimated as the  $E_i$  region between (i) the largest  $E_{i0}$  having zero-value ELA data (i.e.,  $E_{i0} \leq e\Phi_C$ ) located just below the first “positively risen” ion data point  $E_{i+}$  (i.e.,  $E_{i+} > e\Phi_C$ ) and (ii) the  $E_{i+}$  position itself. Moreover, the  $\Phi_C$  regime is also optimized using the zero-cross position  $E_{iR}$  determined from the dashed curve (i.e., the least-squares fit to the data [see Figs. 6(b)–6(d)] by using the shifted Max-

wellian model function<sup>25</sup>). In Fig. 5(a),  $\Phi_C$  data are finally plotted in the regime between  $E_{i0}$  and  $E_{iR}$  [see vertical lines in Figs. 6(b)–6(d)].

Some additional data in Fig. 6 are obtained from the movable IES ELA at (e)  $r_c = 11.9$  cm, (f) 7.6 cm, and (g) 9.0 cm in the absence of ECH along with data for (h) 8.2 cm in the presence of ECH. For the data analysis, the dotted raw data points are at first averaged out using around ten data in order to reduce the fluctuation level of the raw data, which are affected by incident electrons with a few keV (this is equivalent to time-averaging because of the temporal sinusoidal scan of  $E_i$  for the data). This method is well known as a digital filtering technique for low-pass filtering. The magnitudes of the frequency responses of the “moving-average technique” for various data points are exemplified in Fig. 6(a). The averaged data are plotted using green squares in Figs. 6(e)–6(h); that is, each square plotted for  $E_i$  represents the averaged value of  $I_m(E_i) = (2s+1)^{-1} \sum_{u=-s}^s I_{m+u}$ , where  $I_{m-1}$  and  $I_{m+1}$  denote the raw data values in front and behind the data of  $I_m$ , respectively, for  $2s+1$  ( $\equiv n$ )-point averaging. Further data smoothing of the plotted green square is again processed by regression analysis according to the model function of the current-voltage characteristics,<sup>25</sup> i.e.,  $I = I_e + I_0 \exp[-e(E_i - e\Phi_C)/T_i]$  in the region of  $E_i \geq e\Phi_C$ , and  $I = I_e + I_0$  in  $E_i < e\Phi_C$  for the movable IES ELA.<sup>25</sup> Here,  $I_e$  denotes an undesirable shift of the entire curve, which can occur from electronic noise and the above-described electron stray currents. The exponential part in  $E_i \geq e\Phi_C$  resulting from the regression analysis is calculated first. In order to justify each exponential fit in Figs. 6(e)–6(h), the  $\chi^2$  and the correlation coefficient tests for “goodness of fit”<sup>21,26</sup> at the significance levels of 0.05 and 0.01, respectively,<sup>21,26</sup> are applied. The statistical procedure for testing the fits is also usefully employed to assess and optimize  $n$  for the square plots. On the other hand, horizontal brown lines (i.e.,  $I_e + I_0$  in  $E_i < e\Phi_C$ ), which correspond to the maximum and minimum values of the averaged square-shaped data points, are drawn. Here, the minimum digit (or the significant figure) for the horizontal lines is determined from the electronic stray-noise level of  $1 \times 10^{-5}$  A/cm<sup>2</sup> for the ELA currents. This small level does not essentially affect the overall fitting characteristics in Fig. 5. The crossing points of the exponential curve and the horizontal lines thereby yield the plotted  $\Phi_C$  regime in Fig. 5(a). It is also of use to find a “shoulder”  $\Phi_C$  in  $E_i$  (Refs. 19 and 25) from the envelope of the raw data [see the top dashed curve with the circles for the shoulder in Figs. 6(e)–6(h)].

The above-described “double-smoothing” method using both data averaging and regression analysis is tested in Figs. 6(e) and 6(g). According to the model function of  $I$ ,<sup>25</sup> the ideal data points without incident electrons and ion turbulent fluctuations are plotted in Fig. 6(e) as crosses ( $\times$ ), which have the same  $E_i$  intervals as those for the raw-data points (dots). Therefore, the crosses lie on the model function of the exponential regression curve and the two horizontal lines. The yellow filled circles in Fig. 6(e) are averaged similarly to the real averaged data (squares). The yellow points trace well and confirm the model functional shape of the shifted Maxwellian,<sup>25</sup> even when averaging  $\sim 15$  data. In addition,

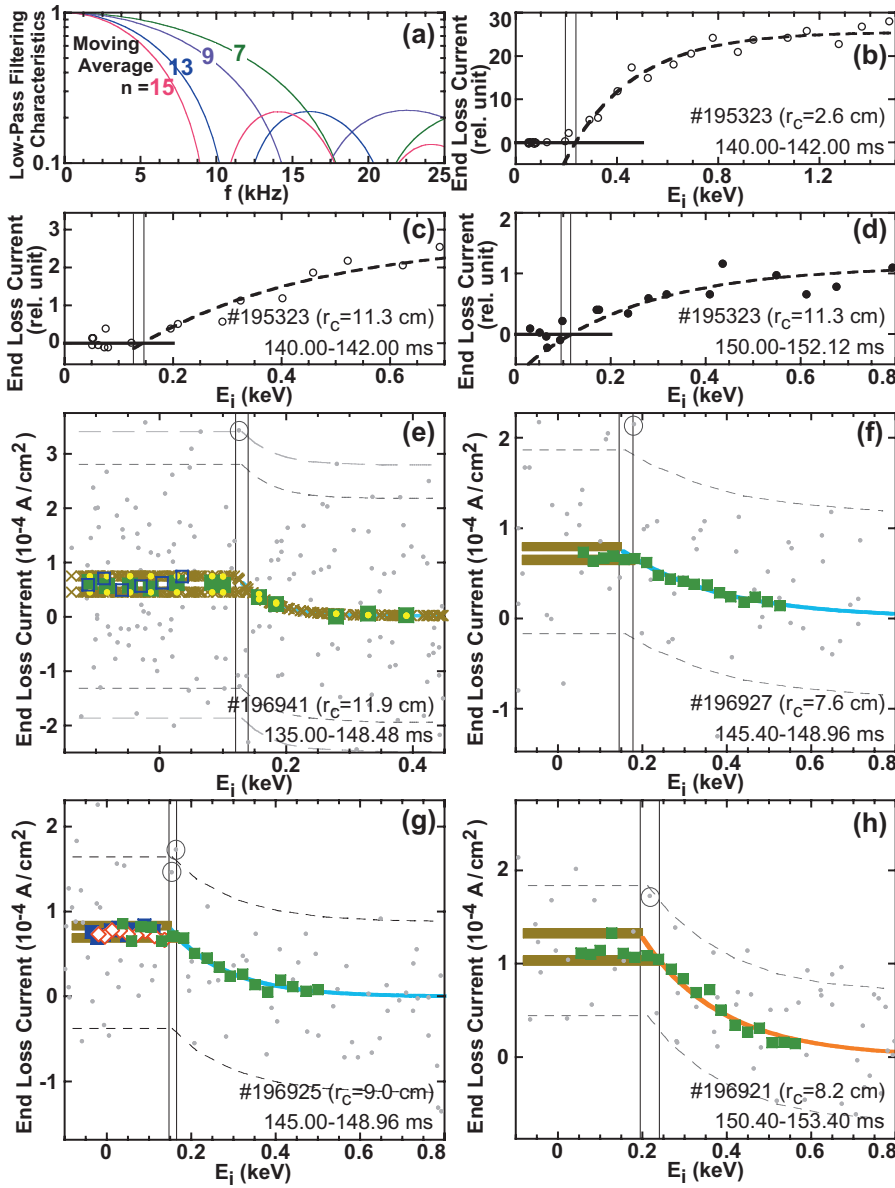


FIG. 6. (Color) The magnitudes of the frequency responses of the “moving average” over various  $n$  data points are exemplified in (a) [i.e., a digital filtering technique that acts as a low-pass filter]. Characteristic tests in (e) and (g) confirm the validity of this method of obtaining the  $\Phi_C$  regime (see the text), where the optimum  $n$  is chosen so as to minimize the discrepancy from the model functional curve. For optimizing  $n$ , the iteration is made until the square plots pass the  $\chi^2$  and the correlation coefficient tests for goodness of fit [see Ref. 21]. For more detail, see the text. The raw data from the IES ELA array [(b)–(d)] and the movable IES ELA [(e)–(h)] are exemplified for the cases without [(b), (c), (e), (f), (g)] and with the energetic-electron layer [(d) and (h)], with the labeled  $r_c$  locations and sampling durations, along with the vertical thin solid lines for the  $\Phi_C$  regime. The raw data (dotted points) in (e)–(h) are at first averaged out. Moreover, the green square points are again processed by regression analysis to attain the exponential fit. In short, the crossing points of the exponential regression curve and the horizontal lines through the maximum and the minimum values of the squares yield the  $\Phi_C$  regime in Fig. 5(a).

13-point averaging data (blue open squares) are plotted, indicating the good fit to the model plot (crosses) in Fig. 6(e). Figure 6(g) also confirms similar fitting characteristics even for the averaging of 7 (green), 13 (blue), and 15 (red) raw data points. These plots well satisfy the narrow  $\Phi_C$  regime of 0.15–0.17 keV. The optimum  $n$  for the green square plots depends on the temporal irregularity of the noise and turbulence on the data. Until we obtain the data, that pass the statistical goodness-of-fit test,<sup>21</sup>  $n$  is varied. Here, we perform the correlation coefficient tests at the 0.01 level of significance<sup>21,26</sup> to justify the use of the fit. The characteristic tests in Figs. 6(e) and 6(g) confirm the validity of the employed analysis method to obtain the  $\Phi_C$  regime. Here, the statistical “outlier”<sup>21</sup> square points in  $E_i < e\Phi_C$  are generally averaged out, and lie convergently between the horizontal lines, when averaging with the above-described optimized  $n$ . In a few instances, one outlier caused by an irregular electron burst is ignored, since it yields an extraordinary jump in  $\Phi_C$  and  $E_r$  [i.e., unexpected  $>150\%$  larger  $E_r$  ( $\approx 8$  kV/m) than

the maximum value in the radial profile of  $E_r$  with ECH], or it disappears at the next data-sampling duration.

The humped profile of  $\Phi_C$  in Fig. 5(a) results in the sign changes of the  $\Phi_C$  gradient (i.e.,  $E_r$ ) near the  $\Phi_C$  peak at  $r_c \approx 7$  cm  $\equiv r_p$ . It is again noted that the opposite  $E_r \times B$  azimuthal ( $\varphi$ -directed) sheared flows near  $r_c = r_p$  separate the plasmas into two regions at  $r_c = r_p$ . This feature of the angular velocity ( $\Omega$ ) reversal from positive to negative near  $r_c = r_p$  is represented in Fig. 5(b) by the thick solid curve.

Further essential features can be seen in the behaviors of the radial plots of the  $E_r$  shear [Fig. 5(c)] and the so-called *dynamic vorticity*  $W$  [Fig. 5(d)].<sup>5,6</sup> It provides a natural generalization of the conventional vorticity vector  $\mathbf{w} = \nabla \times \mathbf{V}$  (i.e., the canonical momentum and the measure of velocity shear in the dynamics of incompressible fluids with uniform density). The  $z$  component of the normalized dynamic vorticity, i.e.,  $W = [\nabla \times (nV_E)]_z / n_0 = d/dr_c(nr_c^2\Omega) / (n_0r_c)$ , is chosen to characterize the  $E \times B$  velocity ( $V_E$ ) shear with

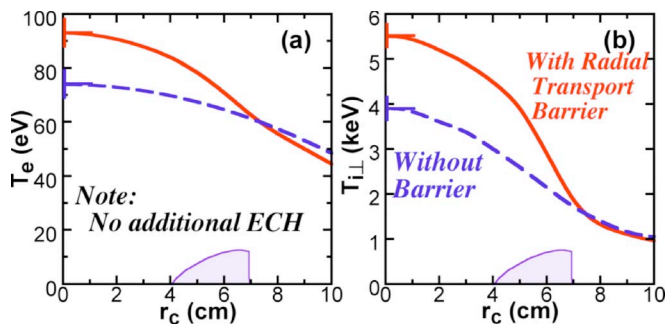


FIG. 7. (Color online) The solid and dashed curves show the (a)  $T_e$  and (b)  $T_i$  profiles from the x-ray and charge-exchange particle analyses with and without the energetic-electron layer (see shaded regions), respectively. Steep  $T_e$  and  $T_i$  gradients in a large-value  $W$  regime along with rather flat and higher  $T_e$  and  $T_i$  values in the internal region surrounded by the layer are found. Neither a plug nor a central-cell ECH is injected.

strongly nonuniform plasma density in our experiments, where  $n_0$  defines the on-axis density. In the presence of the layer, the humped  $\Phi_C$  profile with rapid changes in  $\Omega$  provides significant humps in the  $dE_r/dr_c$  and  $W$  profiles in Figs. 5(c) and 5(d), respectively. A large-value  $W$  regime with a hump (at least in the regime of  $5.5 < r_c \leq 10$  cm), centered near  $r_c = 7$  cm, covers the radii with a remarkable reduction in turbulence fluctuations [see Figs. 2–4]. On the other hand, the high-level fluctuations in the core plasma corresponds to the weakly sheared small-value  $W$  regime at  $r_c < 4$  cm.

This qualitative discussion is based on the usefulness of the  $E_r$  shear for reducing turbulence phenomena.<sup>1–6,22,23</sup> For more detail, we estimate here the possible fitting regime of the maximum and minimum  $E_r$  shear curves using  $\Phi_C$  in Fig. 5(a). The model function needed to estimate the  $E_r$  shear with the fitting extremes in the regression analysis is employed in the form of  $dE_r/dr_c = -A(r_c - a)$  for  $r_c > 7$  cm because of the expected peak position of the shear at  $r_c \approx 7$  cm as described above. From  $E_r = -d\Phi_C/dr_c$ ,  $\Phi_C(r_c)$  is expressed as a double-integration form of the above  $dE_r/dr_c$  with two regression coefficients,  $A$  and  $a$ . By using the set of maximum and minimum values of the  $\Phi_C(r_c)$  data in Fig. 5(a) and  $dE_r/dr_c \approx 0$  at  $r_c = 13$  cm ( $\pm 1$  cm), where  $n_e$  and  $T_e$  have quite low values with a rather flat  $\Phi_C$  profile like those of edge plasmas, we carry out the regression analysis by the use of  $a = 13 + \sin b$ , where  $b$  is an unknown regression coefficient. The analyzed regression curves lead to the two thin solid curves in Figs. 5(b)–5(d), which are consistent with those in Fig. 5(a). The large-value regime in the shear profile cover the  $r_c$  region with reduced turbulence. Various fitting functions are also tested, and show similar peaked profiles in both  $E_r$  shear and vorticity, which cover the turbulence-reduced region with an accuracy of around 1 cm.

The  $T_e$  and  $T_i$  profiles obtained by the x-ray and charge-exchange particle analyses are shown in Figs. 7(a) and 7(b), respectively. One can see steeper gradients for both  $T_e$  and  $T_i$  in the layer ( $5 < r_c < 8$  cm) having large  $E_r$  shear and  $W$  [Figs. 5(c) and 5(d)], along with the resulting higher  $T_e$  and  $T_i$  in the internal region surrounded by this steep gradient layer. Such steep temperature gradients localized in the high-

vorticity layer and accompanied by the temperature enhancement near the axis look very similar to the transport-barrier formation in toroidal devices.<sup>1,2</sup>

#### IV. TURBULENT STRUCTURES, CROSS-FIELD HEAT, AND PARTICLE FLUXES

The characteristic property of transport-barrier formation can be obtained from the analysis of actual cross-field plasma transport. Typically, cross-field particle and energy fluxes in GAMMA 10 are essentially smaller than the longitudinal losses and vary appreciably with  $r_c$ . The actual values of the cross-field fluxes are calculated using local flux-tube-averaged particle and energy balance equations for ions and electrons,<sup>3,20</sup> taking into account the actual particle and energy sources, longitudinal axial losses, and experimentally measured radial profiles including almost unchanged  $n_c$  values, modified  $T_i$  and  $T_e$  gradients [Fig. 7], and the thermal energy fluxes  $q$  (having time variations within a factor of 2), before and during the barrier formation with the time variations of the parameters.

To reveal the transport barrier formation, we should compare these fluxes with the background collisional diffusive fluxes calculated for the measured parameters. The radial particle fluxes are found to be ambipolar in the standard regimes with floating coaxial end plates, and the neoclassical effects caused by the incompletely axisymmetric anchor cell contribute weakly to the radial fluxes.<sup>27</sup> Thus, we can consider that there is pure classical background radial transport in the effectively axisymmetric magnetic field, and use the results of Braginskii.<sup>28</sup> There is an analogy with the neoclassical background transport in the banana regime of tokamaks, since, in the axisymmetrized model, GAMMA 10 can be considered a system with a pure “poloidal” magnetic field. The ion gyroradius in such systems has the same size as the banana width in tokamaks with the same poloidal field. Thus, the background transports in the two systems are qualitatively similar.

Following Ref. 28, the total classical thermal energy fluxes for ions and electrons  $q_{i,e}^{cl}$  consist of fluxes due to the heat conduction  $q_{i,e}^{conduct} = -n_{i,e}\chi_{i,e}\nabla T_{i,e}$  (or thermal fluxes) and convective fluxes  $q_{i,e}^{conv} = (5/2)T_{i,e}J_{i,e}$ , which include thermal energy convections and pressure works. In a steady magnetic field, the particle fluxes  $J_{i,e}$  correspond to the classical particle diffusion through the magnetic field and result from the collisional resistivity.

In the present operation of GAMMA 10 with a high hot-ion-to-electron temperature ratio ( $T_h/T_e \approx 50$ ), we have the particle diffusion coefficient  $D_n \sim 6\chi_h \sim 11\chi_e$ , since the diffusion results from the plasma resistivity and is proportional to a high  $T_h$  and inversely proportional to a small  $T_e^{3/2}$ . This means that in the case of a high  $T_h/T_e$  ratio and a high-density gradient, the convective thermal energy fluxes are the dominant energy fluxes for both electrons and ions. Taking into account the convective thermal energy fluxes as the dominant contribution to both the electron and the ion energy flux, we illustrate the transport barriers using the radial profiles of the energy flux ratios ( $q_h^{exp}/q_h^{cl}$ ) and ( $q_e^{exp}/q_e^{cl}$ ), instead of the respective traditional diffusivity ratios

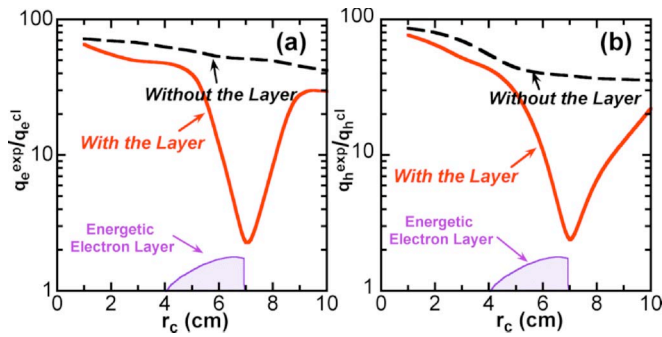


FIG. 8. (Color online) The ratios of the experimentally measured radial energy fluxes to the classical collisional energy fluxes are shown for the regime with the high-vorticity layer (solid curves) and without the layer (dashed curve) for (a) electrons ( $q_e^{\text{exp}}/q_e^{\text{cl}}$ ) and (b) hot ions ( $q_h^{\text{exp}}/q_h^{\text{cl}}$ ). Significant reductions in these ratios are found in both (a) and (b).

( $\chi_h^{\text{exp}}/\chi_h^{\text{cl}}$ ) and ( $\chi_e^{\text{exp}}/\chi_e^{\text{cl}}$ ). The energy-flux-ratio profiles are presented in Fig. 8. Outside the high-vorticity layer or in the regime without the layer, both ( $q_h^{\text{exp}}/q_h^{\text{cl}}$ ) and ( $q_e^{\text{exp}}/q_e^{\text{cl}}$ ) have large values and vary very smoothly [see Fig. 8]. The values of  $q_h^{\text{exp}}$  and  $q_e^{\text{exp}}$  in these cases correspond to the effective  $\chi_h^{\text{eff}}$  and  $\chi_e^{\text{eff}}$  on the order of 0.2 and 0.1 m<sup>2</sup>/s, respectively.

In contrast to the above-described region, the profiles of both ( $q_h^{\text{exp}}/q_h^{\text{cl}}$ ) and ( $q_e^{\text{exp}}/q_e^{\text{cl}}$ ) demonstrate a considerable decrease in the high-vorticity layer, where  $q_h^{\text{exp}}$  and  $q_e^{\text{exp}}$  drop down almost to their classical values. This behavior of  $q_h^{\text{exp}}$  and  $q_e^{\text{exp}}$  correlates with the steeper  $T_e$  and  $T_i$  profiles in Fig. 7 and the turbulence reduction within the high-vorticity layer ( $5.5 < r_c \leq 10$  cm). These results allow us to conclude that a transport barrier (i.e., ITB) is formed in the hot-core plasma of GAMMA 10. The observed ITB is essentially similar to the ITBs in tokamaks.

Here, it should also be noted that the LF turbulence and the associated cross-field plasma transport in mirror-based systems can be self-consistently simulated by means of a special code based on adiabatically reduced magnetohydrodynamiclike equations.<sup>29</sup> The first results of the LF-turbulence simulations in mirrors show a qualitative agreement with the above experimental observations (see Ref. 30). Further detailed studies of the effects of the Kelvin-Helmholtz instability and the Reynolds stress response from the viewpoint of the magnetic-shear effects, for instance, are planned to generalize the turbulence mechanisms in various types of devices.

## V. SUMMARY

The externally controlled formation of an internal transport barrier is observed in GAMMA 10.<sup>5,6</sup> The transverse energy-transport barrier is localized within a layer having a strongly sheared  $\mathbf{E}_r \times \mathbf{B}$  plasma rotation ( $5.5 < r_c \leq 10$  cm).

The high-vorticity layer is formed and maintained by off-axis ECH, which generates a cylindrical layer ( $4 < r_c < 7$  cm) with a high-energy electron population throughout the whole device. The off-axis ECH modifies the initial Gaussian potential profile  $\Phi_C(r_c)$  into a nonmonotonic profile with a hump structure, which leads to the strong shear formation.

The effects of shear formation on turbulent plasmas are demonstrated using the contour modification of the central-cell soft x-ray data [compare Figs. 2(b) and 2(d)] along with the results of the frequency analysis of the soft x-ray and IES ELA data (Figs. 3 and 4). In the internal regions ( $r_c < 5$  cm) having a higher plasma pressure, spatially and temporally varying intermittently turbulent structures are evident [Figs. 2(b) and 2(d)], whereas the formation of the sheared-rotation layer results in a considerable reduction in turbulence within the layer ( $5.5 < r_c \leq 10$  cm).

The local gradients of  $T_i$  and  $T_e$  are appreciably enhanced in the transport barrier layer as in the ITBs of tokamaks and stellarators. Reductions of the effective ion and electron thermal diffusivities are obtained in the barrier layer.

- <sup>1</sup>M. L. Watkins and JET EFDA Contributors, in *Proceedings of the International Atomic Energy Agency (IAEA) Fusion Energy Conference*, Chengdu, 2006 (IAEA, Vienna, 2006), Paper No. IAEA-CN-149/OV/1-3; M. R. Wade and DIII-D Team, *ibid.*, Paper No. IAEA-CN-149/OV/1-4.
- <sup>2</sup>T. Shimozuma, S. Kubo, H. Idei, S. Inagaki, N. Tamura, T. Tokuzawa, T. Morisaki, K. Y. Watanabe, K. Ida, I. Yamada, K. Narihara, S. Muto, M. Yokoyama, Y. Yoshimura, T. Notake, K. Ohkubo, T. Seki, K. Saito, R. Kumazawa, T. Mutoh, T. Watari, A. Komori, and the LHD Experimental Group, *Nucl. Fusion* **45**, 1396 (2005).
- <sup>3</sup>T. Cho, M. Yoshida, J. Kohagura, M. Hirata, T. Numakura, H. Higaki, H. Hojo, M. Ichimura, K. Ishii, K. Md. Islam, A. Itakura, I. Katanuma, Y. Nakashima, T. Saito, Y. Tatematsu, M. Yoshikawa, Y. Kojima, S. Tokioka, N. Yokoyama, Y. Tomii, T. Imai, V. P. Pastukhov, S. Miyoshi, and GAMMA 10 Group, *Phys. Rev. Lett.* **94**, 085002 (2005).
- <sup>4</sup>T. Cho, J. Kohagura, M. Hirata, T. Numakura, H. Higaki, H. Hojo, M. Ichimura, K. Ishii, K. Md. Islam, A. Itakura, I. Katanuma, Y. Nakashima, T. Saito, Y. Tatematsu, M. Yoshikawa, Y. Takemura, A. Kojima, T. Kobayashi, Y. Yamaguchi, Y. Miyata, N. Yokoyama, Y. Tomii, Y. Miyake, S. Kiminami, K. Shimizu, Y. Kubota, H. Saimaru, Y. Higashizono, A. Mase, Y. Yasaka, K. Ogura, K. Sakamoto, M. Yoshida, V. P. Pastukhov, T. Imai, S. Miyoshi, and GAMMA 10 Group, *Nucl. Fusion* **45**, 1650 (2005).
- <sup>5</sup>T. Cho, J. Kohagura, T. Numakura, M. Hirata, H. Higaki, H. Hojo, M. Ichimura, K. Ishii, K. Md. Islam, A. Itakura, I. Katanuma, R. Minami, Y. Nakashima, T. Saito, Y. Tatematsu, O. Watanabe, M. Yoshikawa, A. Kojima, Y. Miyake, Y. Miyata, K. Shimizu, Y. Tomii, M. Yoshida, K. Sakamoto, T. Imai, V. P. Pastukhov, S. Miyoshi, and GAMMA 10 Group, *Phys. Rev. Lett.* **97**, 055001 (2006).
- <sup>6</sup>T. Cho, H. Higaki, M. Hirata, H. Hojo, M. Ichimura, K. Ishii, K. Md. Islam, A. Itakura, I. Katanuma, J. Kohagura, R. Minami, Y. Nakashima, T. Numakura, T. Saito, Y. Tatematsu, M. Yoshikawa, O. Watanabe, Y. Kubota, T. Kobayashi, Y. Yamaguchi, Y. Higashizono, Y. Miyata, H. Saimaru, A. Mase, Y. Yasaka, A. Kojima, M. Yoshida, W. Horton, T. Imai, V. P. Pastukhov, S. Miyoshi, and GAMMA 10 Group, in *Proceedings of the International Atomic Energy Agency (IAEA) Fusion Energy Conference*, Chengdu, 2006 (IAEA, Vienna, 2006), Paper No. IAEA-CN-149/EX/P7-14.
- <sup>7</sup>P. W. Terry, *Rev. Mod. Phys.* **72**, 109 (2000).
- <sup>8</sup>P. H. Diamond, S. I. Itoh, K. Itoh, and T. S. Hahm, *Plasma Phys. Controlled Fusion* **47**, R35 (2005).
- <sup>9</sup>F. Wagner, G. Becker, K. Behringer, D. Campbell, A. Eberhagen, W. Engelhardt, G. Fussmann, O. Gehre, J. Gernhardt, G. v. Gierke, G. Haas, M. Huang, F. Karger, M. Keilhacker, O. Klüber, M. Kornherr, K. Lackner, G. Lisitano, G. G. Lister, H. M. Mayer, D. Meisel, E. R. Müller, H. Murmann, H. Niedermeyer, W. Poschenrieder, H. Rapp, H. Röhr, F. Schneider, G. Siller, E. Speth, A. Stäbler, K. H. Steuer, G. Venus, O. Vollmer, and Z. Yü, *Phys. Rev. Lett.* **49**, 1408 (1982).
- <sup>10</sup>E. J. Strait, L. L. Lao, M. E. Mauel, B. W. Rice, T. S. Taylor, K. H. Burrell, M. S. Chu, E. A. Lazarus, T. H. Osborne, S. J. Thompson, and A. D. Turnbull, *Phys. Rev. Lett.* **75**, 4421 (1995).
- <sup>11</sup>C. M. Greenfield, B. Balet, K. H. Burrell, M. S. Chu, J. G. Cordey, J. C. Deboo, N. Deliyannis, E. J. Doyle, R. J. Groebner, G. L. Jackson, S. Konoshima, D. P. O'Brien, L. Porte, C. L. Rettig, T. H. Osborne, H. St. John, A. C. C. Sips, G. M. Staebler, E. J. Strait, P. M. Stufferfield, T. S. Taylor, S. J. Thompson, K. Thomsen, and A. D. Turnbull, *Plasma Phys. Controlled Fusion* **35**, B263 (1993).

- <sup>12</sup>A. Mase, A. Itakura, M. Inutake, K. Ishii, J. H. Jeong, K. Hattori, and S. Miyoshi, *Nucl. Fusion* **31**, 1725 (1991).
- <sup>13</sup>M. Hirata, T. Cho, E. Takahashi, N. Yamaguchi, T. Kondoh, K. Matsuda, S. Aoki, K. Tanaka, H. Maezawa, and S. Miyoshi, *Nucl. Instrum. Methods Phys. Res. B* **66**, 479 (1992).
- <sup>14</sup>T. Numakura, T. Cho, J. Kohagura, M. Hirata, R. Minami, M. Yoshida, Y. Nakashima, T. Tamano, K. Yatsu, and S. Miyoshi, *Plasma Phys. Controlled Fusion* **45**, 807 (2003).
- <sup>15</sup>J. Kohagura, T. Cho, M. Hirata, T. Tamano, K. Yatsu, and S. Miyoshi, *Phys. Rev. E* **56**, 5884 (1997).
- <sup>16</sup>R. Minami, T. Cho, J. Kohagura, M. Hirata, T. Numakura, H. Watanabe, M. Yoshida, Y. Nakashima, M. Ichimura, T. Tamano, K. Yatsu, and S. Miyoshi, *Plasma Phys. Controlled Fusion* **44**, 1363 (2002).
- <sup>17</sup>K. Ishii, M. Kotoku, T. Segawa, I. Katanuma, A. Mase, and S. Miyoshi, *Rev. Sci. Instrum.* **60**, 3270 (1989).
- <sup>18</sup>M. Yoshida, T. Cho, M. Hirata, H. Ito, J. Kohagura, K. Yatsu, and S. Miyoshi, *Rev. Sci. Instrum.* **74**, 1909 (2003).
- <sup>19</sup>T. Cho, M. Inutake, K. Ishii, I. Katanuma, Y. Kiwamoto, A. Mase, Y. Nakashima, T. Saito, N. Yamaguchi, K. Yatsu, M. Hirata, T. Kondoh, H. Sugawara, J. H. Foote, and S. Miyoshi, *Nucl. Fusion* **28**, 2187 (1988).
- <sup>20</sup>T. Cho, J. Kohagura, T. Numakura, M. Hirata, H. Hojo, M. Ichimura, K. Ishii, A. Itakura, I. Katanuma, Y. Nakashima, T. Saito, Y. Tatematsu, M. Yoshikawa, R. Minami, S. Nagashima, M. Yoshida, T. Tamano, K. Yatsu, and S. Miyoshi, *Phys. Rev. Lett.* **86**, 4310 (2001); T. Cho, M. Hirata, K. Ogura, E. Takahashi, T. Kondoh, N. Yamaguchi, K. Masai, K. Hayashi, I. Katanuma, K. Ishii, T. Saito, Y. Kiwamoto, K. Yatsu, and S. Miyoshi, *ibid.* **64**, 1373 (1990).
- <sup>21</sup>W. H. Press, W. T. Vetterling, S. A. Teukolsky, and B. P. Flannery, in *Numerical Recipes in C* (Cambridge University Press, Cambridge, 1988).
- <sup>22</sup>W. Horton, J. C. Perez, T. Carter, and R. Bengtson, *Phys. Plasmas* **12**, 022303 (2005); W. Horton, B. Hu, J. Q. Dong, and P. Zhu, *New J. Phys.* **5**, 14.1 (2003); J. C. Perez, W. Horton, R. D. Bengtson, and T. Carter, *Phys. Plasmas* **13**, 055701 (2006).
- <sup>23</sup>A. M. Batista, I. L. Caldas, S. R. Lopes, R. L. Viana, W. Horton, and P. J. Morrison, *Phys. Plasmas* **13**, 042510 (2006).
- <sup>24</sup>T. Numakura, T. Cho, J. Kohagura, M. Hirata, Y. Tomii, S. Kiminami, K. Shimizu, N. Morimoto, Y. Takahashi, T. Imai, and S. Miyoshi, *Nucl. Instrum. Methods Phys. Res. A* **573**, 53 (2007).
- <sup>25</sup>J. H. Foote and G. D. Porter, *Plasma Phys. Controlled Fusion* **31**, 255 (1989).
- <sup>26</sup>P. R. Bevington, in *Data Reduction and Error Analysis for the Physical Sciences* (McGraw-Hill, New York, 1969).
- <sup>27</sup>I. Katanuma, Y. Kiwamoto, S. Adachi, M. Inutake, K. Ishii, K. Yatsu, K. Sawada, and S. Miyoshi, *Nucl. Fusion* **27**, 2041 (1987).
- <sup>28</sup>S. I. Braginskii, in *Reviews of Plasma Physics*, edited by M. A. Leontovich (Consultants Bureau, New York, 1965), Vol. 1.
- <sup>29</sup>V. P. Pastukhov, *Plasma Phys. Rep.* **31**, 577 (2005).
- <sup>30</sup>V. P. Pastukhov and N. V. Chudin, *Fusion Sci. Technol.* **51**, 34 (2007).